Imbalance of ionic conductances contributes to diverse symptoms of demyelination

Jay S. Coggan[a,1], Steven A. Prescott[b], Thomas M. Bartol[a], and Terrence J. Sejnowski[a,c,1]

[a]Howard Hughes Medical Institute, The Salk Institute for Biological Studies, La Jolla, CA 92037; [b]Department of Neurobiology and Pittsburgh Center for Pain Research, University of Pittsburgh, PA 15213; and [c]Division of Biological Sciences, University of California at San Diego, La Jolla, CA 92093

This contribution is part of the special series of Inaugural Articles by members of the National Academy of Sciences elected in 2010.

Contributed by Terrence J. Sejnowski, September 30, 2010 (sent for review July 17, 2010)

Fast axonal conduction of action potentials in mammals relies on myelin insulation. Demyelination can cause slowed, blocked, desynchronized, or paradoxically excessive spiking that underlies the symptoms observed in demyelination diseases. The diversity and timing of such symptoms are poorly understood, often intermittent, and uncorrelated with disease progress. We modeled the effects of demyelination (and secondary remodeling) on intrinsic axonal excitability using Hodgkin–Huxley and reduced Morris–Lecar models. Simulations and analysis suggested a simple explanation for the breadth of symptoms and revealed that the ratio of sodium to leak conductance, g_{Na}/g_L, acted as a four-way switch controlling excitability patterns that included spike failure, single spike transmission, afterdischarge, and spontaneous spiking. Failure occurred when this ratio fell below a threshold value. Afterdischarge occurred at g_{Na}/g_L just below the threshold for spontaneous spiking and required a slow inward current that allowed for two stable attractor states, one corresponding to quiescence and the other to repetitive spiking. A neuron prone to afterdischarge could function normally unless it was switched to its "pathological" attractor state; thus, although the underlying pathology may develop slowly by continuous changes in membrane conductances, a discontinuous change in axonal excitability can occur and lead to paroxysmal symptoms. We conclude that tonic and paroxysmal positive symptoms as well as negative symptoms may be a consequence of varying degrees of imbalance between g_{Na} and g_L after demyelination. The KCNK family of g_L potassium channels may be an important target for new drugs to treat the symptoms of demyelination.

axon | Hodgkin–Huxley model | leak conductance | Morris-Lecar model | multiple sclerosis

Oligodendrocytes and Schwann cells tightly wrap axons at regular intervals to form the myelin sheath that allows for rapid axonal conduction. Neuropathies involving axonal demyelination are characterized by the unraveling of this insulation and can affect both the central nervous system, as in the case of multiple sclerosis (MS), and the peripheral nervous system, as in Guillain-Barré syndrome.

Causes of demyelination include immunologic disease processes, as well as lesions such as traumatic nerve damage, nonpenetrating spinal cord injuries, and chronic nerve compression (1–4). Regardless of the precise etiology, clinical presentation often involves negative (loss-of-function) symptoms, including loss of motor control (i.e., paresis) and sensory deficits such as blindness and numbness, as well as positive (gain-of-function) symptoms, including muscle spasms, tactile allodynia, and chronic pain that is constant or paroxysmal (1, 4–7). Which muscles or sensory modalities are affected depends on where in the nervous system the demyelinating lesions develop, but changes in conduction velocity alone are clearly insufficient to explain the breadth of symptoms observed, especially the positive ones. In particular, MS often produces confounding symptoms that can present intermittently, resolving and returning in a way that is decoupled from myelination status and include asymptomatic partial demyelination (clinicoradiographic dissociation; refs. 8–12).

Because remyelination in the central nervous system is minimal and symptoms are not strictly correlated with demyelination, any recovery or continued function despite demyelination suggests compensatory plasticity in the demyelinated membrane (10, 11). Indeed, partially demyelinated axons can recover the ability to conduct through a centimeter or more of demyelination in the optic nerve (13). The diverse clinical symptoms described above could result from axonal excitability changes causing conduction slowing or failure, stimulus-dependent afterdischarge (AD), and spontaneous spiking (9–11). An open question is whether these axonal excitability changes and their associated clinical manifestations reflect a single, common pathogenic process or whether each type of symptom (e.g., negative vs. positive, tonic vs. paroxysmal, etc.) reflects a distinct pathogenic process.

Demyelination is known to destabilize the densities of ionic conductances in affected regions (14–16). Most studies have focused on voltage-gated Na channels and K channels, but the possible contribution of leak currents (voltage-independent K channels) is relatively unexplored (17). Here, we demonstrate using simulations and dynamical analyses that a single mechanism controlling the balance of sodium and leak conductance is sufficient to explain the full range of demyelination symptoms by producing a four-way switch in axonal excitability. The models make testable predictions and have broad implications for understanding regulation of axonal excitability.

Results

Hodgkin–Huxley Model Exhibits a Four-Way Switch in Spiking Pattern as g_{Na}/g_L Ratio Is Varied. We constructed a multicompartmental Hodgkin–Huxley (HH) model of an axon that included the major ion channels found in most axons (g_{Na}, g_L, g_K, and g_{Nap}). The model included a 2-mm length of demyelination halfway along its length (*Methods*). A single action potential was elicited in the soma to assess its propagation across the demyelinated region under various conditions. Modulating g_L in the demyelinated region led to four distinct outcomes: failure of the elicited spike to traverse the demyelinated region (Fig. 1*A*), faithful propagation of the spike across the demyelinated region (Fig. 1*B*), induction of AD (i.e., the single evoked spike triggered continuous autonomous spiking; Fig. 1*C*), and spontaneous firing that originated in the demyelinated region independent of the evoked spike (Fig. 1*D*).

Because spike initiation depends on the values of both g_L and g_{Na}, we systematically varied g_{Na} and g_L in the demyelinated zone without changing g_K or g_{Nap}. In this way, we produced an

Author contributions: J.S.C., S.A.P., T.M.B., and T.J.S. designed research; J.S.C. and S.A.P. performed research; J.S.C. and S.A.P. analyzed data; and J.S.C., S.A.P., and T.J.S. wrote the paper.

The authors declare no conflict of interest.

Freely available online through the PNAS open access option.

[1]To whom correspondence may be addressed. E-mail: coggan@salk.edu or sejnowski@salk.edu.

This article contains supporting information online at www.pnas.org/lookup/suppl/doi:10.1073/pnas.1013798107/-/DCSupplemental.

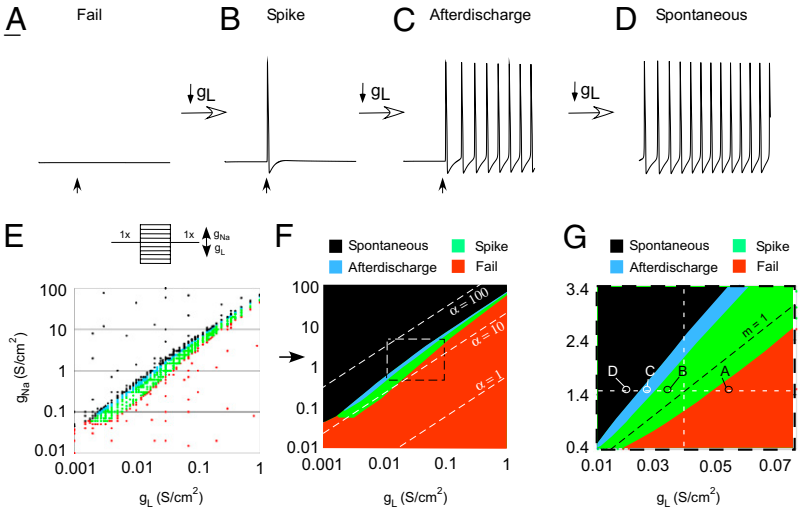

Fig. 1. HH model exhibits a four-way switch in spiking pattern when conductances in its demyelinated region are varied. Four distinct excitation states were obtained by varying the relative amount of g_L. (*A*) Demyelinated region that fails to conduct an action potential owing to high g_L. (*B*) Same demyelinated region that initially failed to conduct a single invading spike successfully propagated a spike when g_L was lowered. (*C*) Further reduction in g_L produced AD (in response to a stimulus that evoked an initial action potential) and (*D*) spontaneous activity (not requiring an external stimulus). (*E*) Phase diagrams determined by the $\alpha = g_{Na}/g_L$ ratio. Color of each point (g_{Na}, g_L) in the phase diagram indicates the state of excitability of the demyelinated axon: Fail (red), single-spike (green), AD (blue), and spontaneous (black). (*F*) Excitability diagram with color-coded areas derived from corresponding points in *E* and α ratios of 1, 10, and 100 marked (dashed lines). (*G*) Expanded region of biological interest on excitability map. Vertical and horizontal dashed lines show how all four excitation phases are crossed whether g_L or g_{Na} is modified. Dashed line with slope m = 1 shows stability in spike generation when g_L and g_{Na} covary.

excitation map with clear phase transition boundaries (Fig. 1*E*), from which a phase diagram could be deduced (Fig. 1*F*). Closer examination of the physiological range of conductances (Fig. 1*G*) revealed that all four excitability patterns could be induced whether g_L (horizontal dashed line) or g_{Na} (vertical dashed line) were varied. In contrast, concurrent modulation of both conductances along a diagonal line with positive slope tended to maintain balance without switching the type of excitability. Thus, the ratio $\alpha = g_{Na}/g_L$, which is a measure of the balance between depolarizing and hyperpolarizing mechanisms, provides insight into the cause of the observed four-way switch in spiking pattern and the pathogenic consequences of improper conductance balance in axonopathy.

Replication of AD and Spontaneous Spiking in a Reduced Morris–Lecar Model. Spike failure at low α values occurred because current shunt prevented the membrane from charging to threshold. We further investigated AD and spontaneous spiking in a single-compartment Morris–Lecar (ML) model to identify which cellular properties are necessary and sufficient for each pattern, and to elucidate how the necessary cellular properties interact to produce each pattern.

The initial reduced ML model (without g_{Nap}) comprised only two variables to isolate basic mechanisms (*Methods*). The phase plane in Fig. 2*A* shows the fast activation variable *V* plotted against the slower recovery variable *w*. When displaced from its stable fixed point by a perturbation, the system produced a single spike as it returned to its stable fixed point. When α was increased, that stable fixed point was destroyed through a saddle-node on invariant circle (SNIC) bifurcation; in the absence of that stable point, the system entered a limit cycle and spiked spontaneously (Fig. 2*B*). By systematically varying g_{Na} (Fig. 2*C*), to change α, we produced bifurcation diagrams that show how the system transitions from normal to spontaneous spiking. Bifurcation analysis confirmed that the model transitioned directly from normal spiking to spontaneous spiking without any intermediate parameter range associated with AD (*SI Text* provides an investigation of bistability in 2D ML models; Figs. S1 and S2).

To make the ML model more similar to the HH model, we added a persistent sodium current (g_{Nap}). Because g_{Nap} operates on a longer time scale than the other currents in the 2D ML model, the resulting model is 3D. This 3D ML model exhibited robust AD (Fig. 2*D*) comparable to that observed in the HH model (compare Fig. 1). Bifurcation analysis identified a parameter range within which the stable fixed point and the stable limit cycle overlapped (Fig. 2*E*), corresponding to the range of parameter values for which the 3D model exhibited AD (Fig. 2*D*). The bifurcation diagram in Fig. 2*F* confirmed that even for "control" values of g_{Na} and g_L, there are intermediate values of g_{Nap} that produce AD. These results demonstrate that g_{Nap} is necessary for AD but not for spontaneous spiking in our ML model; furthermore, g_{Nap} is not sufficient to produce AD insofar as AD also depends on the values of g_{Na} and g_L and requires a perturbation (i.e., at least one evoked spike).

We then used phase plane analysis to explore how g_{Nap} impacts spike generation (Fig. 2*G*). Activation of g_{Nap}, which is controlled by *z*, can be understood from the *V*-*z* phase plane: for g_{Nap} values associated with spontaneous spiking, the *V*- and *z*-nullclines do not intersect at a stable fixed point, which means *z* increases without restriction. In contrast, for g_{Nap} values not associated with spontaneous spiking, the *V*- and *z*-nullclines intersect at a stable fixed point at which *z* will stabilize (Fig. 3*A*). Spike generation triggered by g_{Nap} activation can be understood from the *V*-*w* phase plane: for starting conditions ($z = 0$), the *V*- and *w*-nullclines intersect at a stable fixed point, but as *z* increases (which causes g_{Nap} to contribute an increasingly large depolarizing current), the *V*-nullcline shifts upward, eventually causing the fixed point to lose stability through a Hopf bifurcation, whereupon the neuron spikes repetitively. The generation of individual spikes is best understood from the *V*-*w* plane, but the overall initiation of repetitive spiking is best understood from the *V*-*z* plane; therefore, we focused on the *V*-*z* plane for all subsequent phase plane analysis.

Dynamical Explanation of AD. We next examined the dynamical basis for AD in the 3D ML model. For parameter values not associated with spontaneous spiking, the *V*- and *z*-nullclines intersect at three points, two of which are labeled on Fig. 3*A*. A single spike is produced after a perturbation as the system returns to its stable fixed point. AD results when the system does not return to its stable fixed point after a perturbation, as explained below. If g_{Na} is increased (Fig. 3*B*, *Left*) or g_L is decreased (Fig. 3*C*, *Left*), the evoked spike is followed by AD unless the change in g_{Na} or g_L is balanced by a compensatory change in g_L or g_{Na}, respectively (Fig. 3 *B* and *C*, *Right*). Consistent with Fig. 2*F*, AD can also occur if g_{Nap} itself is increased (Fig. 3*D*). In all cases of AD, the *V*-*z* trajectory looks like the sample response shown in the phase plane in Fig. 3*D* (see also Fig. S3). Unlike in Fig. 3*A*, where the trajectory comes back around to intersect the *V*-nullcline below the saddle point (arrowhead) and then continues to the stable node, in Fig. 3*D* the trajectory comes back above the saddle point and then enters a stable limit cycle. This is a direct consequence of bistability, in which the system may converge on

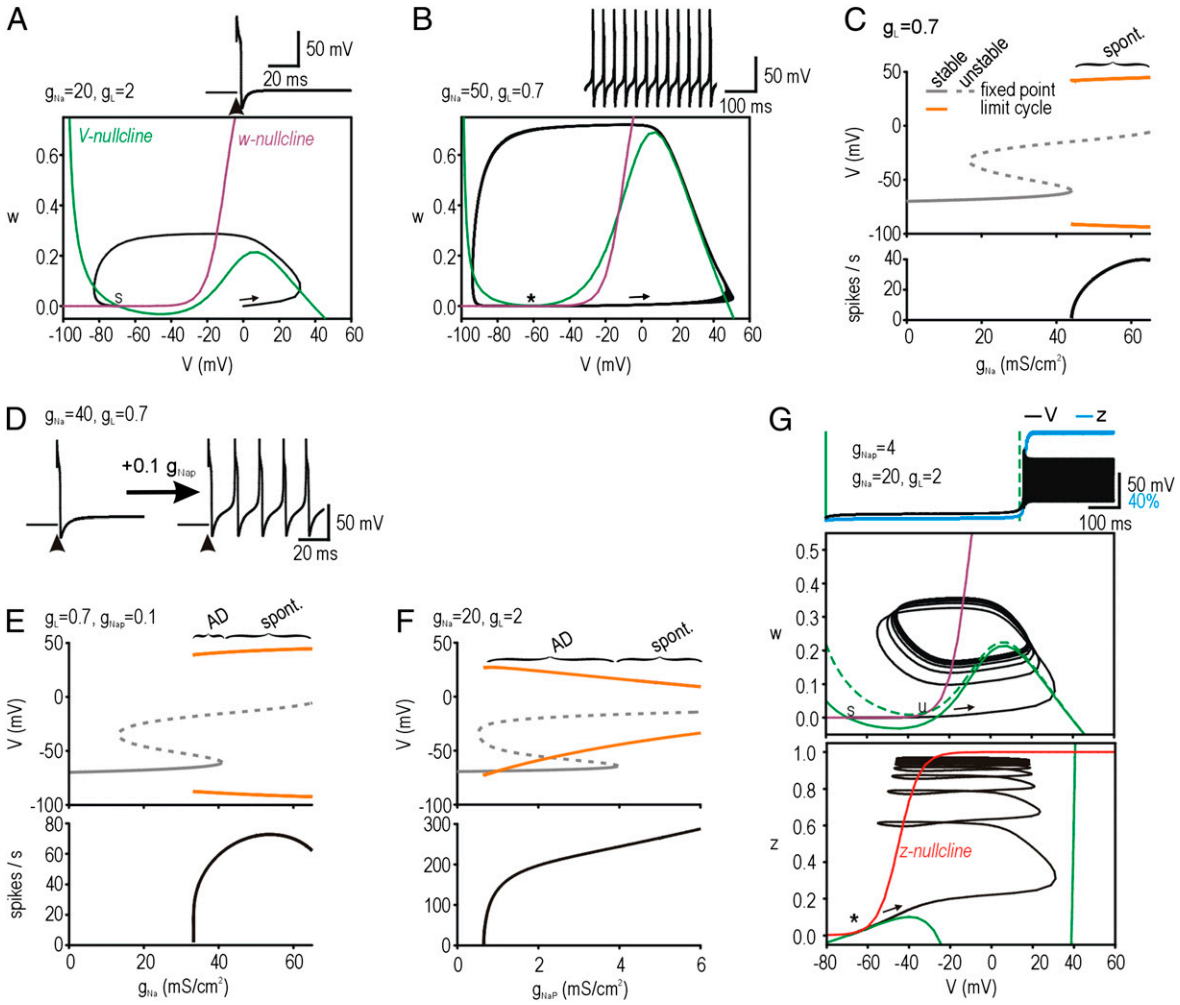

Fig. 2. Requirements for spontaneous spiking and AD in the ML model. (*A*) Phase-plane representation of evoked spike in ML model without g_{Nap} and with g_{Na} and g_L set to default values, as indicated on figure (in mS/cm^2). Spike was evoked by instantaneously resetting *V* to 0 mV (time indicated by black arrowhead), whereupon it returns to the stable fixed point (*s*) identified by the intersection between the *V*-nullcline (green line) and the *w*-nullcline (maroon line). In this and all other phase planes, direction of the trajectory (black line) is indicated by a black arrow. (*B*) When g_{Na} is increased and/or g_L is decreased sufficiently that the nullclines no longer intersect at a stable fixed point (*), the ML model spikes spontaneously. (*C*) Bifurcation diagram determined by fixing g_L and varying g_{Na}, to determine the exact value of g_{Na} at which the stable fixed point was destroyed through a SNIC bifurcation, beyond which spontaneous spiking (*spont*) occurs. *Upper: V* at the fixed point (gray line) and at the maximum and minimum of the limit cycle (orange lines). *Lower:* Frequency of spiking associated with the limit cycle. (*D*) *Left:* Perturbation (arrowhead) evoked a single action potential. *Right:* AD could be evoked in the ML model only when g_{Nap} was added. (*E*) Repeat of bifurcation analysis in *C* but now with g_{Nap} in the model. The same SNIC bifurcation is evident, but now the limit cycle extends to the left of that bifurcation, producing a region of bistability in which AD can occur. (*F*) Bifurcation analysis in which g_{Nap} was increased shows the same pattern as in *E* but with a wider region of bistability. (*G*) *Top:* Simulation showing spontaneous spiking in ML model with g_{Nap} showing *V* (black line) and *z* (blue line). *Middle: V*- and *w*-nullclines start by intersecting at a stable fixed point (*s*) but that point eventually becomes unstable (*u*) through a Hopf bifurcation as the *V*-nullcline shifts (dashed green line) because of increases in z. In reality, the *w*-nullcline shifts slowly during the time leading up to the bifurcation. The timing of that bifurcation is indicated by a dashed green vertical line on the time series (*Top*). *Bottom:* The shift in the *w*-nullcline is caused by progressive activation of g_{Nap} (controlled by *z*), as evident from the *V*-*z* nullcline. For parameters causing spontaneous spiking in this 3D model, the *V*- and *z*-nullclines do not intersect at a stable fixed point (*). Although spikes are generated by the interaction between *V* and *w*, the onset of that spiking is controlled by interaction between the fastest and slowest variables and is therefore evident on the *V*-*z* phase plane.

either of its stable "attractors" after a perturbation. AD results from the system converging on a stable limit cycle rather than the coexisting stable fixed point. The saddle point defines the boundary separating the basins of attraction around each attractor. The postspike value of *z* relative to this boundary dictates whether g_{Nap} sustains depolarization sufficiently to maintain activation of g_{Nap} (thus initiating AD) or whether it fails to sustain its own activation (thus allowing the system to return to its resting state). This can also be seen in the time course of *z* (blue lines) in Fig. 3 *A–D*.

Having established that AD is a direct consequence of bistability associated with the presence of g_{Nap}, we divided the problem into two questions: how strongly must g_{Nap} be activated to cause repetitive spiking, and is g_{Nap} activated sufficiently (after a single evoked spike) to cause repetitive spiking? We addressed the first question by systematically varying *z* from 0 to 1 to determine at what value repetitive spiking would occur. By treating *z* as a bifurcation parameter rather than as a variable, the model was reduced from 3D to 2D. For a model with g_{Nap} less than 0.1 mS/cm^2, no amount of activation would provoke AD (for the g_{Na} and g_L values tested) (Fig. 3*Ei*); the response from the 3D ML model is superimposed on the bifurcation diagram and shows a single spike after perturbation. If g_{Nap} was increased to 0.8 mS/cm^2, repetitive spiking would occur if *z* exceeds ≈0.55 (Fig. 3*Eii*); however, the response from the 3D ML model shows that the

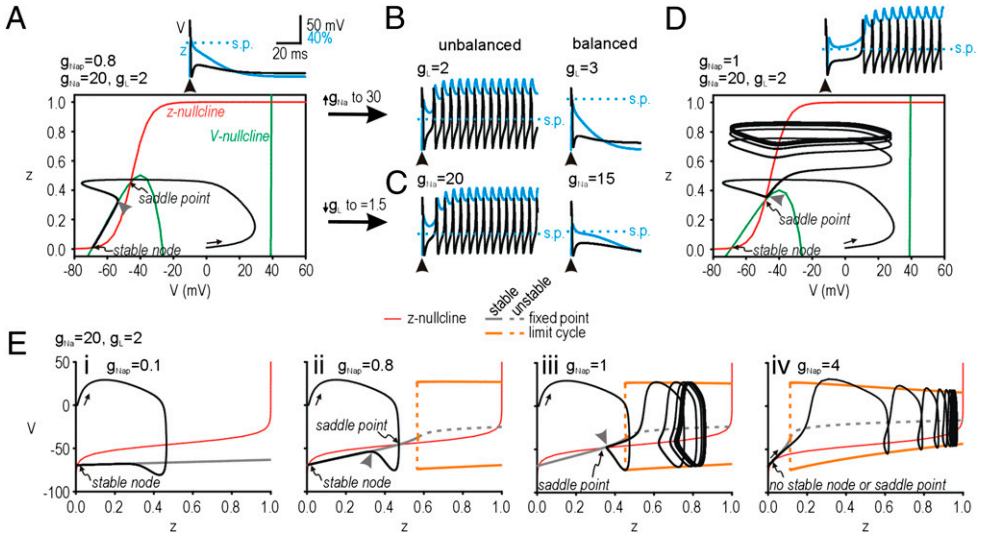

Fig. 3. AD is a manifestation of bistability. (*A*) *Upper:* Time course of *V* (black line) and *z* (blue line). *Lower:* *V*-*z* phase plane showing single evoked spike. Note that *V*- and *z*-nullclines intersect at two labeled points. The *V*-*z* trajectory passes above the saddle point but returns to the green nullcline below it (gray arrowhead), whereupon the trajectory is directed back to the stable node. The *z* value of the saddle point (*sp*) is indicated by a dotted blue line on the time series (*Upper*). (*B*) Increasing g_{Na} leads to AD (*Left*) unless there is a balanced increase in g_L (*Right*). (*C*) Similarly, decreasing g_L leads to AD (*Left*) unless there is a balanced decrease in g_{Na} (*Right*). In all instances without AD (*A*–*C*), *z* decreases below the saddle point after the evoked spike, whereas it remains above the saddle point in those instances when AD occurs. This is also true for AD caused by increasing g_{Nap}. (*D*) *Upper:* Time course of *V* (black line) and *z* (blue line). *Lower:* The *V*-*z* phase plane shows the trajectory passing above the saddle point (gray arrowhead), whereupon it enters a stable limit cycle rather than returning to the fixed point. Thus, the saddle point represents the boundary between two basins of attraction; one attractor corresponds to quiescence and the other to repetitive spiking. The evoked spike is a perturbation that may or may not knock the system from its quiescent attractor to its repetitive spiking attractor; that transition depends on the *z* trajectory relative to the saddle point. (*E*) For these bifurcation diagrams, *z* was treated as a variable and systematically increased to determine the value at which it would cause a Hopf bifurcation. This was repeated for different values of g_{Nap} in *i*–*iv*. Trajectories from corresponding 3D models (i.e., with *z* treated as a variable) are superimposed in black. The *z* nullcline is also shown in red because its intersection with the bifurcation diagram reveals the stable node and saddle point, as indicated. (*i*) For the lowest value of g_{Nap}, no increase in *z* was sufficient to cause a bifurcation and, as predicted, only a single spike is produced before the trajectory returns to the stable node. (*ii*) For the next-higher value of g_{Nap}, increasing *z* high enough can cause a bifurcation, but the perturbation caused by a single evoked spike was not sufficient for *z* to remain above (i.e., to the right of) the saddle point; trajectory returned to the stable branch of bifurcation diagram at point indicated by arrowhead. (*iii*) For the next-higher value of g_{Nap}, a bifurcation as in *b* was observed, but this time the *z* trajectory remained above the saddle point, whereupon it crossed the bifurcation, resulting in AD. (*iv*) For a value of g_{Nap} known to cause spontaneous spiking, the *z*-nullcline does not intersect the stable branch of the bifurcation diagram and, as a result, the trajectory passes through the bifurcation in the absence of any stimulus.

perturbation caused by one spike did not produce sufficient activation. The trajectory converged back on the stable branch of the bifurcation diagram to the left of the saddle point (defined by where the bifurcation diagram and *z*-nullcline intersect). If g_{Nap} was further increased to 1 mS/cm^2, repetitive spiking would occur if *z* exceeded ≈0.45 (Fig. 3*Eiii*); the response from the 3D model shows that this level of activation can indeed be evoked by a single spike. Unlike in Fig. 3*Eii*, the trajectory in Fig. 3*Eiii* converged back to the stable branch of the bifurcation diagram to the right of the saddle point, thus allowing the trajectory to enter into the limit cycle rather than being directed back to the stable node. When g_{Nap} was increased to 4 mS/cm^2, minimal activation of g_{Nap} was required to provoke repetitive spiking (Fig. 3*Eiv*); in fact, the *z*-nullcline did not even intersect the bifurcation diagram in its stable branch, which is consistent with the saddle point and stable node being absent under those conditions (Fig. 2 *F* and *G*), thus allowing the model to fire spontaneously.

Role of g_{Nap} in AD. Dynamical systems analysis indicates that g_{Nap} is necessary to produce AD in our ML model, and predicts that g_{Nap} might also be required for AD in the HH model. We tested this prediction in our multicompartment HH model as well as in a reduced HH model (*Methods*). We began with the latter because, by reducing our full HH model to a homogeneous single compartment, we were able to apply bifurcation analysis. Systematically varying g_{Na} in our reduced HH model without g_{Nap} revealed a narrow region of bistability (Fig. 4A) reminiscent of that associated with a subcritical Hopf bifurcation in the ML model (Fig. S1). Simulations confirmed that AD occurred for parameter values associated with bistability (Fig. 4*A*). Although adding g_{Nap} broadened the bistable region (Fig. 4*B*), the results of Fig. 4*A* argue that g_{Nap} is not required for certain forms of AD. The g_{Nap}-independent AD in Fig. 4*A* is a consequence of positive feedback activation of I_{Na} outrunning the negative feedback mediated by I_K (see *SI Text*); therefore, we predicted that speeding up activation of I_K would prevent this g_{Nap}-independent AD, which was indeed the case (Fig. 4*C*, *Left*). Adding g_{Nap} to that model gave g_{Nap}-dependent AD (Fig. 4*C*, *Right*) and confirmed that g_{Nap} is sufficient to allow AD given the appropriate g_{Na}/g_L ratio.

We then proceeded with testing the role of g_{Nap} for AD in the full HH model. Removing g_{Nap} abolished AD (Fig. 5*A*). Using the model in Fig. 5*A* (i.e., without g_{Nap}), we systematically increased α in a manner akin to bifurcation analysis (Fig. 2*C*) and found that the model transitioned directly from single spike to spontaneous spiking (Fig. 5*B*); that is, there was no range of α associated with AD when g_{Nap} was lacking (see also Fig. 5*C*). Although consistent with the ML model, this result is inconsistent with the g_{Nap} -independent AD observed in the reduced HH model. The most likely explanation is that the inward current in the demyelinated region is shunted to adjoining, less-excitable regions; this would tend to significantly blunt fast positive feedback mediated by I_{Na} while having less impact on slow positive feedback mediated by I_{Nap}, thus compromising g_{Nap}-independent AD without substantially effecting g_{Nap}-dependent AD. These spatial effects are not accounted for in the reduced HH model. Overall, data in Fig. 5 indicate that AD in the full HH model depends on slow positive feedback mediated by g_{Nap}.

Conditions for Triggering AD. As explained in Fig. 3, there are two requirements for AD: (*i*) that the system is bistable, and (*ii*) that the system is forced from one to another basin of attraction. Bifurcation analysis of AD in the ML model demonstrated that there are parameter values for which AD would occur if g_{Nap} were sufficiently activated, but such activation of g_{Nap} was not achieved after a single spike (Fig. 3*Eb*); in other words, the system was bistable but the perturbation was insufficient to force the system

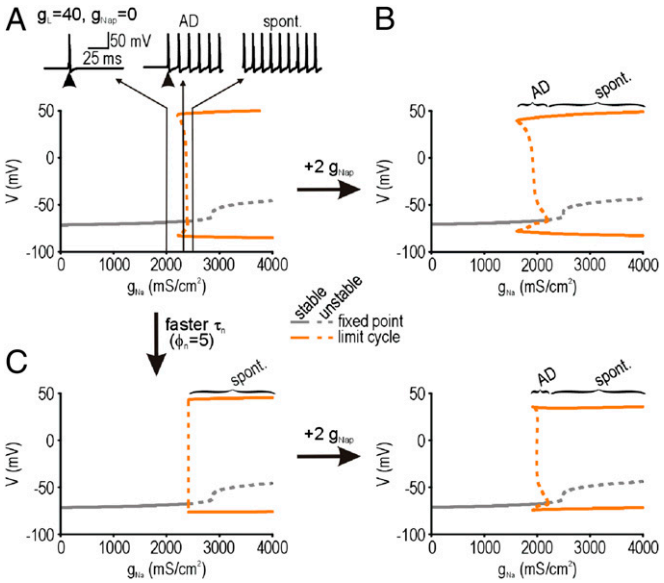

Fig. 4. Bifurcation analysis in a spatially reduced HH model. (*A*) Systematically varying g_{Na} in our reduced HH model without g_{Nap} revealed a narrow region of bistability similar to that seen in the ML model in Fig. S1. Simulations confirmed that a short pulse (50 μA/cm^2) could trigger AD with model parameters within the range associated with bistability. (*B*) Adding g_{Nap} to the model in *A* broadened the range of g_{Na} over which bistability occurs. Bistability in *A* depends on positive feedback activation of I_{Na} outrunning the negative feedback mediated by I_K; accordingly, g_{Nap}-independent AD was prevented by speeding up the rate of activation of I_K by dividing τ_n by a factor Φ_n (*C*, *Left*). Adding g_{Nap} to this monostable model resulted in bistability (*Right*), thus confirming that g_{nap} is sufficient to allow AD given the appropriate g_{Na}/g_L ratio.

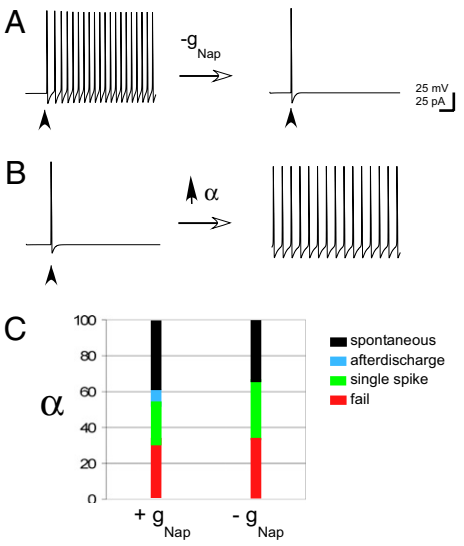

Fig. 5. Afterdischarge in the full HH model requires g_{Nap}. (*A*) Without changing any other parameters, removing g_{Nap} from a full HH model that exhibited AD changed that model's response to a single spike pattern. (*B*) In the absence of g_{Nap}, systematically increasing α caused excitability to change directly from single spike to spontaneous, without any parameter range associated with AD. (*C*) Influence of g_{Nap} on the boundaries of α. AD phase disappears with elimination of g_{Nap} from the demyelinated zone.

to its second attractor. This finding predicts that multiple perturbations could cause cumulative activation of g_{Nap} (i.e., cumulative increases in z) sufficient to provoke AD. This prediction was tested first by applying multiple perturbations to an ML model that, in principle, should be able to produce AD if g_{Nap} were sufficiently activated. Phase plane and bifurcation analyses demonstrated that AD was triggered by the V-z trajectory crossing over the saddle point into the basin of attraction for the stable limit cycle for a train of three stimuli at 10-ms intervals or a train of six stimuli at 30-ms intervals (Fig. 6*A*).

We next tested the effects of repeated stimulation on reduced HH models, specifically to contrast g_{Nap}-independent and -dependent AD. Because the positive feedback responsible for the former is fast, we predicted that AD would not be triggered by slow repeated perturbations because the effects of each perturbation would be "forgotten" by the time the next perturbation occurred (given the fast intrinsic kinetics). As predicted, in the model exhibiting g_{Nap}-independent AD (Fig. 6*B*, *Left*), AD could be elicited by a single pulse but could not be elicited, even by repetitive stimulation, when g_{Na} was slightly reduced (top and middle traces). In contrast, for the model exhibiting g_{Nap}-dependent AD (Fig. 6*B*, *Right*), stimulation with as few as three pulses elicited AD (middle trace) for g_{Na} values where a single pulse could not (top trace). In the latter model, a single pulse still failed to elicit AD even after a sizeable increase in g_{Na} (Fig. 6*B*, *Right*, bottom trace), implicating the relative importance of *slow* cumulative activation of g_{Nap}.

On the basis of results in Fig. 5 indicating that AD in the full HH model is g_{Nap} dependent, we predicted that repeated stimulation would facilitate the triggering of AD in the full HH model. To test this, we stimulated the axon at a value of α for which the demyelinated region only responded to a single stimulus with a single spike. Two sequential pulses at 10-ms intervals evoked two spikes in the demyelinated region. But with three stimulus spikes (also 10-ms intervals) the demyelinated region responded with AD (Fig. 6*C*, *Left*). Further testing the relationship between spike number and frequency, as in the ML model, we challenged the axon with three spikes and six spikes at 30-ms intervals. At this rate, as few as six stimuli were required to produce cumulative activation of g_{Nap} sufficient to produce AD in the demyelinated region (Fig. 6*C*, *Right*). These results matched the predictions of the ML model and support the hypothesis that cumulative activation of g_{Nap} (blue lines in Fig. 6*C*) underlies the "wind up" to AD.

Discussion

We have demonstrated in a computational model of a demyelinated axon that varying the ratio $\alpha = g_{Na}/g_L$ can cause transitions between distinct axonal spiking patterns (failure, single-spike, AD, and spontaneous), thereby functioning as a four-way switch of intrinsic excitability. Such a rapid and dynamic switching mechanism provides a parsimonious yet robust explanation for the full range of symptoms associated with demyelination disorders, from negative symptoms to paroxysmal and tonic positive symptoms (10, 18–20).

The α ratio governs spike initiation by linking critical passive (g_L) and active (g_{Na}) membrane conductance components. Because of its instantaneous kinetics, g_L continuously influences spike threshold and, therefore, is more important than the delayed rectifier g_K for spike initiation (*SI Text*). Regulating g_L could control axon excitability (synergistically with g_{Na}) in the course of demyelination and its sequalae (21, 22). Although AD and bistability have been described in more complex systems (23, 24), and other factors including impedance mismatch (itself related to local input resistance) contribute to excitability in a spatially extended model (25), our model demonstrates the sufficiency of g_{Na}/g_L (in the presence of g_{Nap}) to explain four excitability states that may underlie the positive and negative symptoms of demyelination. Furthermore, given that qualitative excitability changes can result from small changes in α, the intermittence of symptoms may reflect operation of the axon near one of its critical transition boundaries.

We investigated the mechanisms underlying AD and spontaneous activity in a reduced model amenable to dynamical systems analysis. Our 2D ML model exhibited spontaneous spiking when α

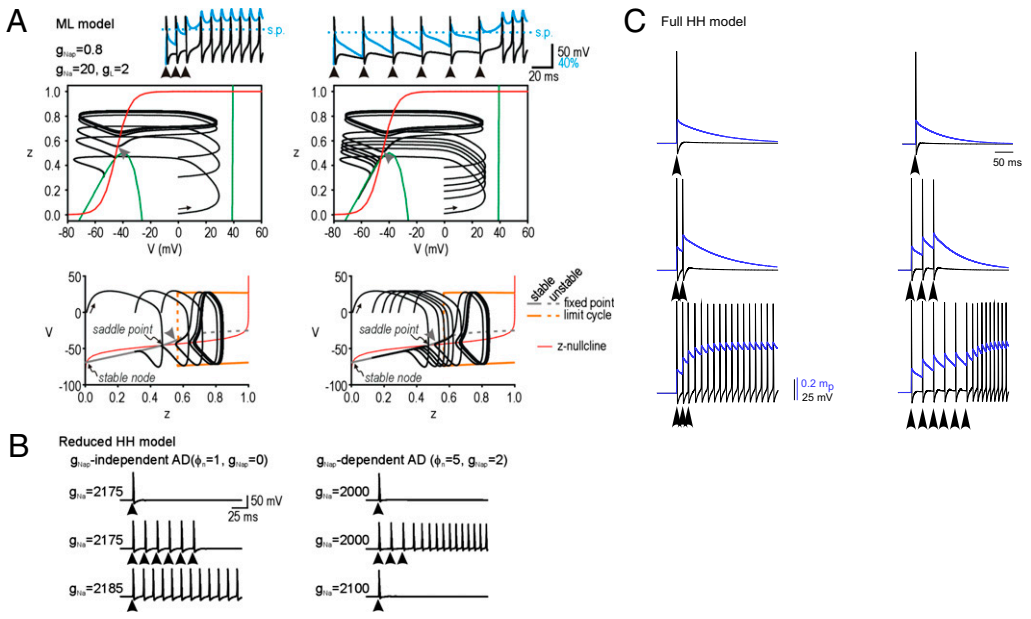

Fig. 6. Triggering of g_{Nap}-dependent AD is facilitated by repeated spikes. Bifurcation analysis in Fig. 3*Eii* showed that a "repetitive spiking" attractor may exist for a given set of parameters but that a single evoked spike may not be sufficient to knock the system to that attractor. If so, a larger perturbation (e.g., multiple spikes) could, in principle, trigger AD. (*A*) Simulations (*Top*) show the minimum number of evoked spikes required to trigger AD in the ML model when evoked spikes are delivered at 10-ms or 30-ms intervals (*Left* and *Right*, respectively). Phase planes (*Middle*) and bifurcation diagrams (*Bottom*) confirm that AD does not occur until *z* rises and remains above (gray arrowheads) the saddle point. *(B)* Effects of repeated stimulation in the reduced HH models depend on the type of AD. In the model exhibiting g_{Nap}-independent AD (*Left*), AD could be triggered by a single pulse when g_{Na} was 2,185 mS/cm^2 (bottom trace) but could not be elicited, even by repetitive stimulation at a 25-ms interval, when g_{Na} was slightly reduced to 2,175 mS/cm^2 (top and middle traces). In contrast, for the model exhibiting g_{Nap}-dependent AD (*Right*), stimulation with as few as three pulses elicited AD (middle trace) for g_{Na} values where a single pulse could not (top trace). In the latter model, a single pulse still failed to elicit AD even after a sizeable increase in g_{Na} (bottom trace). (*C*) Corresponding simulations done in the full HH model with g_{Nap}. Consistent with g_{Nap}-dependent AD, a train of stimuli delivered at 10-ms or 30-ms intervals (arrowheads) triggered AD after three and six stimuli, respectively.

was increased sufficiently to destabilize the system, but the 2D ML model could not exhibit AD comparable to that seen in the demyelinated HH model (Fig. 2 and Figs. S1 and S2). Robust AD required g_{Nap}. Bifurcation analysis of the 3D ML model revealed a region of bistability: AD occurs when, after a perturbation, the system converges on its limit cycle attractor rather than its coexisting fixed point attractor. The persistent Na current constitutes an "ultra"-slow positive feedback process that must outlast the slow negative feedback responsible for afterhyperpolarization (AHP); AD occurs when g_{Nap} remains sufficiently activated (above a saddle-point threshold) after an AHP, such that net membrane current is inward and drives autonomous spiking. A more thorough analysis of the dynamics of g_{Nap} feedback, comparable in nature to that performed by Verduzco-Flores et al. (26) in the context of network dynamics, would be an interesting focus of future investigation.

By understanding the nonlinear mechanisms, we were able to make specific testable predictions. First, we predicted that an ultraslow positive feedback mechanism, such as that provided by g_{Nap}, is necessary for AD but not for spontaneous spiking. This prediction was confirmed in simulations in which g_{Nap} was removed from our HH model (Fig. 5). Furthermore, we predicted that g_{Nap}, although necessary, is not sufficient to produce AD; specifically, g_{Nap} must be activated strongly enough that it renders net current inward after the AHP. When g_{Nap} is high, a single evoked spike was sufficient to trigger AD, whereas several evoked spikes may be required to trigger AD when g_{Nap} is lower. This prediction was tested and confirmed in both the ML and HH models (Fig. 6). Spontaneous activity, on the other hand, can be achieved more directly with sufficiently high α, even in the absence of g_{Nap}. The number of spikes required to provoke AD depended on the frequency of evoked spikes and the susceptibility of the axon. This shows that an occult pathological state can exist in a seemingly normal neuron, only to manifest its influence after the appropriate trigger, which matches the pattern of paroxysmal symptoms.

An injured axon has a limited arsenal of countermeasures to preserve signal propagation. Events taking place during the demyelination process make the α hypothesis a plausible explanation for the diversity of demyelination symptoms. The distribution and balance of ion channels becomes destabilized along with the reorganization of the membrane and its ion channel components (10, 11). In the case of MS-related pathogenic pain, for example, Na channels are targeted by common therapeutics such as carbamazepine (27).

Cellular g_L modulation has been reported in several systems. Leak channels are largely responsible for the dorsal–ventral input resistance gradients that are used in the medial entorhinal cortex to maintain gradients of integration properties in grid cell firing fields (28). The regulation of specific g_L*s* (TASK1) has been implicated in maintaining resting potential, input resistance, and the adaptive response to hypoxia or stroke development. They can be modulated by neurotransmitters and can shut down axon conduction when overactivated by anesthetics (29). The modulation of potassium-mediated leak currents by neurotransmitter has also been observed in autonomic neurons and in central myelinated and unmyelinated nerves (30–32). The involvement of g_L and g_{Na} in oscillatory and ectopic spike activity in axotomized primary sensory neurons has been implicated and fits with our model as an explanation for ectopic pain under these conditions (33). Despite this, leak channels have not been a focus of drug development strategies.

Although most therapies for MS target the immune system, one exception is 4-aminopyridine (4-AP), which is an antagonist of voltage-gated potassium currents (34) whose use is limited by a low safety factor (35). Our model provides a plausible explanation for the low potency and efficacy of 4-AP (see also Fig. S4). At a given resting potential a small number of voltage-gated potassium channels will be open, thus contributing to the local input resistance. A very high dose of antagonist would be needed to close sufficient numbers of voltage-gated potassium channels to have a measurable effect on the cumulative g_L in the membrane. If, as it seems, the traditional use of sodium channel blockers as treatments for positive clinical phenomena in MS has a rational basis (36, 37), we propose that regulation of g_L might also take part in the axonal compensation mechanism and might be an effective pharmacotherapy target.

In summary, we have firmly established the mechanisms underlying four distinct phases of axonal firing during demyelination:

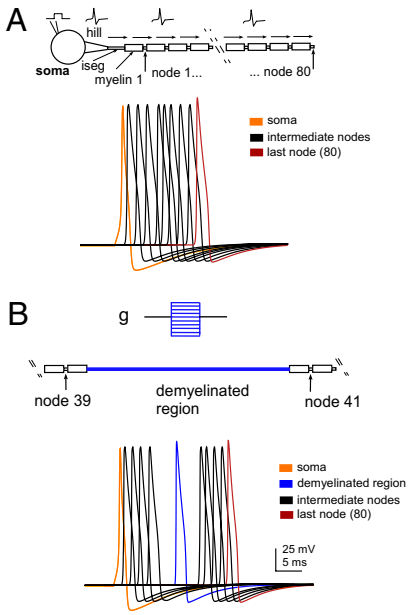

Fig. 7. The axon model. (*A*) Normal myelinated model with soma, axon hillock (hill), initial segment (iseg), and 80 myelin–node of Ranvier pairs. Brief current injection in the soma initiated an action potential that propagated down the axon. Terminal node (brown) and various other nodes (black) are shown. (*B*) Model with demyelinated region inserted at center of model by extending the length of node 40–2,000 μm (blue). The value of g_{Na}, g_{Nap} or g_K was varied only in the demyelinated (blue).

normal spiking, failed conduction, AD, and spontaneous activity. Transitions in axonal excitability caused by varying α indicate that a single mechanism controlling the balance of g_{Na} and g_L is sufficient to explain the diverse set of symptoms associated with demyelination. We propose that selectively modulating members of the KCNK family of leak channels, hitherto unexplored, could alleviate symptoms of MS. Members of this family are also modulated by oxygen tension, pH, mechanical stretch, and G proteins, which suggest additional therapeutic avenues.

Methods

HH Model. A compartmental model of a fast-spiking myelinated axon was created using the NEURON Simulator (http://www.neuron.yale.edu/neuron) (38). Although the ultrastructure of a myelinated axon is quite complex (39), we used a geometrically simplified model to first understand the behaviors in a model with reduced complexity. Saltatory conduction initiated by a single square pulse in the soma was reliably transmitted through the length of the axon, with no attenuation or changes in spike waveform (until the terminal few nodes where the spike increased in amplitude owing to boundary condition wave reflection; Fig. 7*A*). The axon was partially demyelinated by extending the length of a middle node from 1 to 2,000 μm—equivalent to the removal of 10 oligodendrocytes at the center of the axon where the current dynamics are unaffected by boundary conditions (Fig. 7*B*). *SI Text* provides additional model details.

HH-style voltage-gated Kv3.1 (40–42), Nav1.6, Nap (43, 44), and channels were located in the node compartments only. Leak conductance (g_L) was located in all regions except myelinated segments. Corresponding passive and active membrane properties, channel densities, and ion concentrations are listed in Table S1. Estimates for the sodium and potassium channel densities at nodes of Ranvier are ≈1,000 channels/μm^2 (18), but estimates for g_L channel densities at nodes were not available, so we varied channel densities to explore a wide range of combinations.

Simulations. An action potential was evoked by injecting a square current pulse (10 pA, 0.5 ms) into the soma. All simulations were conducted in NEURON using a 10-μs time step.

Rate equations for ion channels. The equations that describe the ion channels used in all of the simulations presented in this article were based on those used in previous studies. The equations for the mammalian voltage-gated Na channels were derived from the ModelDB database (http://senselab.med.yale.edu/modeldb) for ref. 44, and the equations for the mammalian fast voltage-gated potassium channel are from ref. 42.

Nav1.6:

$$I_{Na} = g_{Na} m^3 h (V_m - E_{Na}) \quad [1]$$

$$\alpha_m = \frac{1.76(V_m + 21.4)}{\{1 - e^{[-(V_m+21.4)/10.3]}\}} \quad [2]$$

$$\beta_m = \frac{0.13[-(V_m + 18.7)]}{\{1 - e^{[(V_m+18.7)/9.16]}\}} \quad [3]$$

$$\alpha_h = \frac{0.062[-(V_m + 114)]}{\{1 - e^{[(V_m+114)/11]}\}} \quad [4]$$

$$\beta_h = \frac{1.7}{\{1 + e^{[-(V_m+31.8)/13.4]}\}} \quad [5]$$

Persistent Na:

$$I_{Nap} = g_{Nap} p^3 (V_m - E_{Na}) \quad [6]$$

$$\alpha_p = \frac{0.01(V_m + 27)}{\{1 - e^{[-(V_m+27)/10.2]}\}} \quad [7]$$

$$\beta_p = \frac{0.00025[-(V_m + 34)]}{\{1 - e^{[(V_m+34)/10]}\}} \quad [8]$$

Kv3.1:

$$I_K = g_K n^3 (1 - \gamma + \gamma p)(V_m - E_K) \quad [9]$$

$$\alpha_n = 0.2120 e^{(0.04V)} \quad [10]$$

$$\beta_n = 0.1974 e^{(0V)} \quad [11]$$

$$\alpha_p = 0.00713 e^{(-0.1942V)} \quad [12]$$

$$\beta_p = 0.0935 e^{(0.0058V)} \quad [13]$$

$$\gamma = 0.1 \quad [14]$$

Leak:

$$I_L = g_L (V_m - E_L) \quad [15]$$

Modified ML Model. The phase-plane model is based on the ML model (45, 46) and has been described in detail previously (47). The single-compartment, conductance-based model was governed by

$$\begin{aligned} C\,dV/dt = & -g_{\mathrm{L}}(V - E_{\mathrm{L}}) - \bar{g}_{\mathrm{Na}} m_\infty(V)(V - E_{\mathrm{Na}}) \\ & - \bar{g}_{\mathrm{K}}\, w (V - E_{\mathrm{K}}) - \bar{g}_{\mathrm{Nap}}\, z (V - E_{\mathrm{Na}}) \end{aligned} \quad [16]$$

$$dw/dt = \Phi_w \frac{w_\infty(V) - w}{\tau_{\mathrm{w}}(V)} \quad [17]$$

$$dz/dt = \Phi_z \frac{z_\infty(V) - z}{\tau_z(V)} \quad [18]$$

$$x_\infty(V) = 0.5\left[1 + \tanh\left(\frac{V - \beta_x}{\gamma_x}\right)\right] \quad [19]$$

$$\tau_x(V) = 1/\cosh\left(\frac{V - \beta_x}{2 \cdot \gamma_x}\right), \quad [20]$$

where V is voltage and w and z are variables controlling time- and voltage-dependent activation of g_K and g_{Nap}, respectively; g_{Na} was assumed to activate instantaneously, and m was therefore always at steady state. In Eqs. **19** and **20**, x corresponds to m, w, or z. The following parameters were used in all simulations: $C = 2\ \mu F/cm^2$, $E_L = -70$ mV, $E_{Na} = 50$ mV, $E_K = -100$ mV, $\beta_m = -1.2$ mV, $\gamma_m = 18$ mV, $\beta_w = -10$ mV, $\gamma_w = 10$ mV, $\Phi_w = 0.15$, $\beta_z = -45$ mV, $\gamma_z = 10$ mV, $\Phi_z = 0.05$ (unless otherwise stated), and delayed rectifier potassium conductance $\bar{g}_K = 20\ mS/cm^2$. Leak conductance g_L, fast sodium conductance $\bar{g}_{Na}$, and persistent sodium conductance $\bar{g}_{Nap}$ were varied as indicated in the text. In all simulations reported here, "evoked" spikes were triggered by instantaneously resetting voltage to 0 mV and then letting it evolve freely rather than applying a stimulating current, because the former manipulation produces a spike without any influence from an underlying stimulus; this approximates what occurs when the spike is triggered remotely (as in the HH model).

Equations were numerically integrated in XPP (48) using the Euler method with a 0.05-ms time step. Nullclines were also calculated in XPP. For calculating a nullcline at time t, all variables not associated with the nullcline (e.g., w and z for the V-nullcline) were held constant at their value at time t. Bifurcation analysis was conducted in AUTO using the XPP interface.

Reduced HH Model. To apply bifurcation analysis to the HH model, we reduced our multicompartment HH model to a homogeneous single-compartment model. The six ordinary differential equations describing this spatially reduced model were numerically integrated in XPP using the Runge–Kutta method with a 0.005-ms time step. Bifurcation analysis was conducted in AUTO. All parameter values were the same as for full HH model unless otherwise indicated in the text.

ACKNOWLEDGMENTS. We thank Dr. Daniel X. Keller and Cristina Domnisoru for technical advice and Dr. Roger Tsien for stimulating discussion.

1. Calvin WH, Devor M, Howe JF (1982) Can neuralgias arise from minor demyelination? Spontaneous firing, mechanosensitivity, and afterdischarge from conducting axons. *Exp Neurol* 75:755–763.
2. Kapoor R, Li YG, Smith KJ (1997) Slow sodium-dependent potential oscillations contribute to ectopic firing in mammalian demyelinated axons. *Brain* 120:647–652.
3. Love S, Coakham HB (2001) Trigeminal neuralgia: Pathology and pathogenesis. *Brain* 124:2347–2360.
4. Wang G, Thompson SM (2008) Maladaptive homeostatic plasticity in a rodent model of central pain syndrome: Thalamic hyperexcitability after spinothalamic tract lesions. *J Neurosci* 28:11959–11969.
5. Song XJ, Hu SJ, Greenquist KW, Zhang JM, LaMotte RH (1999) Mechanical and thermal hyperalgesia and ectopic neuronal discharge after chronic compression of dorsal root ganglia. *J Neurophysiol* 82:3347–3358.
6. Liu CN, et al. (2000) Tactile allodynia in the absence of C-fiber activation: Altered firing properties of DRG neurons following spinal nerve injury. *Pain* 85:503–521.
7. Minert A, Gabay E, Dominguez C, Wiesenfeld-Hallin Z, Devor M (2007) Spontaneous pain following spinal nerve injury in mice. *Exp Neurol* 206:220–230.
8. Barkhof F (2002) The clinico-radiological paradox in multiple sclerosis revisited. *Curr Opin Neurol* 15:239–245.
9. Twomey JA, Espir MLE (1980) Paroxysmal symptoms as the first manifestations of multiple sclerosis. *J Neurol Neurosurg Psychiatry* 43:296–304.
10. Rasminsky M (1981) Hyperexcitability of pathologically myelinated axons and positive symptoms in multiple sclerosis. *Adv Neurol* 31:289–297.
11. Waxman SG (1982) Membranes, myelin, and the pathophysiology of multiple sclerosis. *N Engl J Med* 306:1529–1533.
12. Waxman SG, Kocsis JD, Black JA (1995) Pathophysiology of demyelinated axons. *The Axon: Structure, Function, and Pathophysiology*, eds Waxman SG, Kocsis JD, Stys PK (Oxford Univ Press, Oxford), pp 438–461.
13. Ulrich J, Groebke-Lorenz W (1983) The optic nerve in MS: A morphological study with retrospective clinicopathological correlation. *Neuro-Ophthalmology* 3:149–159.
14. Bostock H, Sears TA (1978) The internodal axon membrane: Electrical excitability and continuous conduction in segmental demyelination. *J Physiol* 280:273–301.
15. Smith KJ (2007) Sodium channels and multiple sclerosis: Roles in symptom production, damage and therapy. *Brain Pathol* 17:230–242.
16. Waxman SG (2006) Axonal conduction and injury in multiple sclerosis: The role of sodium channels. *Nat Rev Neurosci* 7:932–941.
17. Beck H, Yaari Y (2008) Plasticity of intrinsic neuronal properties in CNS disorders. *Nat Rev Neurosci* 9:357–369.
18. Bostock H, Grafe P (1985) Activity-dependent excitability changes in normal and demyelinated rat spinal root axons. *J Physiol* 365:239–257.
19. Baker M, Bostock H (1992) Ectopic activity in demyelinated spinal root axons of the rat. *J Physiol* 451:539–552.
20. Baker MD (2000) Axonal flip-flops and oscillators. *Trends Neurosci* 23:514–519.
21. Hines M, Shrager P (1991) A computational test of the requirements for conduction in demyelinated axons. *Restor Neurol Neurosci* 3:81–93.
22. Mainen ZF, Joerges J, Huguenard JR, Sejnowski TJ (1995) A model of spike initiation in neocortical pyramidal neurons. *Neuron* 15:1427–1439.
23. Baldissera F, Cavallari P, Dworzak F (1994) Motor neuron 'bistability'. A pathogenetic mechanism for cramps and myokymia. *Brain* 117:929–939.
24. Kager H, Wadman WJ, Somjen GG (2007) Seizure-like afterdischarges simulated in a model neuron. *J Comput Neurosci* 22:105–128.
25. Waxman SG, Brill MH (1978) Conduction through demyelinated plaques in multiple sclerosis: Computer simulations of facilitation by short internodes. *J Neurol Neurosurg Psychiatry* 41:408–416.
26. Verduzco-Flores S, Ermentrout B, Bodner M (2009) From working memory to epilepsy: Dynamics of facilitation and inhibition in a cortical network. *Chaos* 19:015115.
27. Pöllmann W, Feneberg W (2008) Current management of pain associated with multiple sclerosis. *CNS Drugs* 22:291–324.
28. Garden DLF, Dodson PD, O'Donnell C, White MD, Nolan MF (2008) Tuning of synaptic integration in the medial entorhinal cortex to the organization of grid cell firing fields. *Neuron* 60:875–889.
29. Meuth SG, et al. (2009) The neuroprotective impact of the leak potassium channel TASK1 on stroke development in mice. *Neurobiol Dis* 33:1–11.
30. Coggan JS, Purnyn SL, Knoper SR, Kreulen DL (1994) Muscarinic inhibition of two potassium currents in guinea-pig prevertebral neurons: Differentiation by extracellular cesium. *Neuroscience* 59:349–361.
31. Armett CJ, Ritchie JM (1960) The action of acetylcholine on conduction in mammalian non-myelinated fibres and its prevention by an anticholinesterase. *J Physiol* 152:141–158.
32. Trigo FF, Marty A, Stell BM (2008) Axonal $GABA_A$ receptors. *Eur J Neurosci* 28: 841–848.
33. Amir R, Liu CN, Kocsis JD, Devor M (2002) Oscillatory mechanism in primary sensory neurones. *Brain* 125:421–435.
34. Kocsis JD, Bowe CM, Waxman SG (1986) Different effects of 4-aminopyridine on sensory and motor fibers: Pathogenesis of paresthesias. *Neurology* 36:117–120.
35. Judge SI, Bever CT, Jr. (2006) Potassium channel blockers in multiple sclerosis: Neuronal Kv channels and effects of symptomatic treatment. *Pharmacol Ther* 111: 224–259.
36. Hooge JP, Redekop WK (1995) Trigeminal neuralgia in multiple sclerosis. *Neurology* 45:1294–1296.
37. Sakurai M, Kanazawa I (1999) Positive symptoms in multiple sclerosis: Their treatment with sodium channel blockers, lidocaine and mexiletine. *J Neurol Sci* 162:162–168.
38. Hines ML, Carnevale NT (1997) The NEURON simulation environment. *Neural Comput* 9:1179–1209.
39. Sosinsky GE, et al. (2005) Development of a model for microphysiological simulations: Small nodes of ranvier from peripheral nerves of mice reconstructed by electron tomography. *Neuroinformatics* 3:133–162.
40. Corrette BJ, Repp H, Dreyer F, Schwarz JR (1991) Two types of fast K+ channels in rat myelinated nerve fibres and their sensitivity to dendrotoxin. *Pflugers Arch* 418: 408–416.
41. Devaux J, et al. (2003) Kv3.1b is a novel component of CNS nodes. *J Neurosci* 23: 4509–4518.
42. Wang LY, Gan L, Forsythe ID, Kaczmarek LK (1998) Contribution of the Kv3.1 potassium channel to high-frequency firing in mouse auditory neurones. *J Physiol* 509:183–194.
43. Caldwell JH, Schaller KL, Lasher RS, Peles E, Levinson SR (2000) Sodium channel Na(v) 1.6 is localized at nodes of ranvier, dendrites, and synapses. *Proc Natl Acad Sci USA* 97: 5616–5620.
44. McIntyre CC, Richardson AG, Grill WM (2002) Modeling the excitability of mammalian nerve fibers: Influence of afterpotentials on the recovery cycle. *J Neurophysiol* 87: 995–1006.
45. Morris C, Lecar H (1981) Voltage oscillations in the barnacle giant muscle fiber. *Biophys J* 35:193–213.
46. Rinzel J, Ermentrout GB (1998) Analysis of neural excitability and oscillations. *Methods in Neuronal Modeling: From Ions to Networks*, eds Koch C, Segev I (MIT Press, Cambridge, MA), pp 251–291.
47. Prescott SA, De Koninck Y, Sejnowski TJ (2008) Biophysical basis for three distinct dynamical mechanisms of action potential initiation. *PLOS Comput Biol* 4:e1000198.
48. Ermentrout GB (2002) *Simulating, Analyzing, and Animating Dynamical Systems: A Guide to XPPAUT for Researchers and Students* (Society for Industrial and Applied Mathematics, Philadelphia).